Nanofocusing Performance of Plasmonic Probes based on Gradient Permittivity Materials

Dongxue Wang[1], Ze Zhang[1], Jianwei Wang[1], Ke Ma[2], Hua Gao[1,3] and Xi Wang[2,4]

[1]*School of Science, China University of Geosciences, Beijing 100083, China*

[2]*Department of Materials Science and Engineering, University of Delaware, Newark, DE 19716, USA*

[3]*gaohua@cugb.edu.cn*

[4]*wangxi@udel.edu*

Abstract:

Probe is the core component of an optical scanning probe microscope such as scattering-type scanning near-field optical microscopy (s-SNOM). Its ability of concentrating and localizing light determines the detection sensitivity of nanoscale spectroscopy. In this paper, a novel plasmonic probe made of a gradient permittivity material (GPM) is proposed and its nanofocusing performance is studied theoretically and numerically. Compared with conventional plasmonic probes, this probe has at least two outstanding advantages: First, it doesn't need extra structures for surface plasmon polaritons (SPPs) excitation or localized surface plasmon resonance (LSPR), simplifying the probe system; Second, the inherent nanofocusing effects of the conical probe structure can be further reinforced dramatically by designing the distribution of the probe permittivity. As a result, the strong near-field enhancement and localization at the tip apex improve both spectral sensitivity and spatial resolution of a s-SNOM. We also numerically demonstrate that a GPM probe as well as its enhanced nanofocusing effects can be realized by conventional semiconductor materials with designed doping distributions. The proposed novel plasmonic probe promises to facilitate subsequent nanoscale spectroscopy applications.

Key words: Nanofocusing, Plasmonic probe, gradient permittivity material, surface plasmon polaritons, field enhancement and localization

1. Introduction

Nanoscale spectroscopy using scanning probe microscopes (SPMs) provides topographical and spectral information of samples well below diffraction limits. As a typical SPM, scattering-type scanning near-field optical microscopy (s-SNOM) achieves nano-image mapping by focusing free-space light at the tip apex, which results in significant electromagnetic field enhancement and localization at nanoscale. With this electromagnetic hotspot, s-SNOM could collect both amplitude and phase of scattered light [1-3]. Tip-enhanced Raman spectroscopy (TERS) is similar to s-SNOM but collecting and analyzing the Raman shift of scattered light. With the aid of the hotspot formed at the probe tip, TERS offers high detection sensitivity to single molecule and a high spatial resolution to sub-nanometer, making it one of the most precise modern analytical technique [4, 5]. Atomic force microscopy with infrared spectroscopy (AFM-IR) illuminates a sample with pulses of infrared light, which is absorbed by the sample, resulting in a rapid thermal expansion pulse under the AFM tip. By recording the oscillation amplitude of the AFM tip as a function of incident wavelengths, AFM-IR obtains absorption spectra which are correlated to conventional bulk IR spectra, providing chemical identification [6]. Among various optical SPMs, probe is the crucial element. A conventional probe with metallic coating focuses light from a diffraction-limited optical mode into a nanoscale hotspot at the tip apex, known as the lighting rod effect, to obtain a high enhancement and a small spot size. However, the mode mismatch between the two modes limits the

excitation efficiency and reduces the signal-to-noise ratio of detected signals from the tip apex [5]. To improve its performance, various efforts, involving probe structure optimization [7], probe material exploring [8], coating properties investigation [9, 10], and fabrication engineering [11-13], have been made. Besides the probe itself, other influencing factors such as the polarization properties of the illumination [14-17], substrate coupled properties [7, 18] and surrounding medium [19, 20] have been extensively studied to further improve the detection sensitivity. However, even with these research progress, optical SPMs are still suffering from low excitation and collection efficiencies and high far-field background noise, limiting high-precision detections. Therefore, highly localized light with stronger intensity and smaller spot size at the probe apex is much desirable to suppress interferences with the background illumination and improve the scanning spatial resolution.

In recent years, researchers have introduced two mechanisms, localized surface plasmon resonance (LSPR) and nanofocusing, to improve the probe performance. LSPR concentrates light intensely around sub-wavelength conductive nanoparticles or nanostructures. The resonant wavelengths are strongly dependent on the morphology, size, composition of the nanoparticles or nanostructure, and the local dielectric environment. Various plasmonic probes utilizing LSPR have been demonstrated by different nanostructures, such as tip-integrated bowtie antennas [21, 22], pyramidal tips [23, 24], nanoparticles [25-27], metal-coated fiber tips [28], and tip-sculptured single groove [29].

There are two processes occurring at a nanofocusing plasmonic probe, surface plasmon polaritons (SPPs) excitation and SPPs nanofocusing at the tip apex. Multiple coupling schemes to excite SPPs, such as linear gratings[30], concentric ring gratings [31, 32], tip-connected with photonic crystal structures [33], and optical fibers [34], have been demonstrated. However, few efforts have been made to improve the nanofocusing process. The inherent nanofocusing effect occurring on a tapered or conical probe is termed as ‘adiabatic nanofocusing’, which is the most common method used to smooth out the huge momentum gap between the far field and near field waves [35, 36]. When SPPs propagate along a probe towards the tip apex, their wave vectors increase gradually and smoothly, squeezing the propagating SPPs into non-propagating surface plasmons at the tip apex, because of the peculiar dispersion relation of the probe structure. This nanofocusing effect results from the tapered probe structure, i.e., once the structure is determined, its nanofocusing effect is also determined.

While great achievements have been made on plasmonic probes in recent years, most reported probes utilizing LSPR and nanofocusing are still facing three fundamental challenges. First, introducing nanostructure to excite either LSPR or SPPs to such a small element inevitably increases the complexity for the fabrication of probes. Second, restricted optical alignment, sometimes with complicated external alignment tools, is required to fully take advantages of these SPPs excitation structure. Third, most plasmonic probes are not suitable for mid-infrared wavelengths because plasmonic wavelengths for noble metals operate in visible or near-infrared wavelengths.

To overcome these fundamental challenges, we will use a gradient-index unstructured planar surface to excite SPPs and support the propagation on it [37]. By modulating the distribution of the permittivity, we have demonstrated the electromagnetic field localization and enhancement effects on this kind of gradient-index non-structured planar surface [38]. In this paper, we introduce this SPPs excitation and field localization effect to a probe structure. We design a probe made by gradient permittivity materials (GPMs). Without any excitation structure, SPPs can be excited and propagate on this probe surface. More importantly, in addition to the nanofocusing effect brought by the conical probe structure itself, the propagating speed and the wave vectors of SPPs can be tuned by the distribution of the permittivity,

which enhances the nanofocusing effectively. Thus, a better field enhancement and field localization effect will be obtained by optimizing propagation and radiation losses.

For demonstration purposes, we simulate the nanofocusing effect of GPM probes produced by semiconductor doping method. The results show that, even considering the actual absorption of a doped semiconductor, both field enhancement and localization at the probe apex are improved greatly.

2. SPPs excited on a GPM probe without coupling structure

As mentioned above, usually, to excite SPPs on a plasmonic probe, extra grating or prism couplers are needed to compensate the mismatch of the wave vector between SPPs and free-space light. Here we propose a probe made by GPMs to excite SPPs itself. Illumination on a GPM surface leads to a single layer of electric dipoles to oscillate at the air/GPM interface. The radiating field of single dipoles located on the surface of a GPM is asymmetric due to the variation of local permittivity. Therefore, the amplitudes of excited magnetic field components along the interface with $|k| > k_0$, recognized as surface wave components, are nonzero, indicating free space to SPP coupling [37]. We use a commercial software COMSOL Multiphysics to simulate the interaction between the incident light and the GPM probe to demonstrate that GPM is able to couple free-space light and SPPs for probes. Fig.1(a) gives the schematic illustration of the conical probe and the incident light. The geometry of the probe consists of a cone with height of h = 5 μm, opening at an angle of $\varphi = 30$ degree, ending in a part of a sphere with radius of R = 50 nm. These geometric dimensions are comparable to an actual probe. For clarity, a coordinate system is established, which originates from the apex of the conical probe and the z axis is along the axis of the probe, as shown in Fig. 1(a). A Gaussian beam is incident upon the probe from the left side at an incident angle of $\vartheta = 60$ degree, with the electric field magnitude of $E = 1$ V/m in the plane of incidence (TM polarization). The beam waist and the incident wavelength are set to be 10 μm and 1 μm, respectively. In the following of this paper, the structure of the probe and the condition of the incident light remain unchanged in all calculations unless otherwise specified.

As for the electromagnetic parameters, the permittivity of free space and the probe are set to be ε_1 and ε_2, respectively. For a GPM probe, we use a tanh function to describe its distribution, $\varepsilon_2 = -\delta\tanh(\beta(z - z_0)) + \varepsilon_{r0}$, where the span of the permittivity is set to be $2\delta = 40$, the slope $\beta = 1 \times 10^7/\mathrm{m}$, the center of the permittivity distribution z_0 = 2.5 μm and the average value of the permittivity $\varepsilon_{r0} = -22$. Using a tanh function avoids abrupt changes of permittivity and its derivatives, minimizing scattering effect from singularities. The red solid line in Fig.1(b) depicts the distribution of this gradient permittivity of the probe along the z coordinate. It is seen that there is an obvious permittivity variation region between z = 2 μm and z = 3 μm, within which the permittivity gradually decreases from -2 to -42. Outside this region, the permittivity almost remains to be -42 and -2, respectively, at the top side and bottom side of the probe. For comparison, a constant permittivity $\varepsilon_2 = -20$ is also given, as shown by the black dashed line in Fig.1(b).

As studied before, if an incident electric component is along the direction of the permittivity gradient, SPPs will be excited in the GPM area and propagates along the direction of the gradient [37]. Fig.1(c) gives the distributions of the electric components, where the left column corresponds to the GPM probe, and the right column represents the probe with a constant permittivity. To demonstrate the excitation of SPPs, the distributions of the Ez component in the xz plane are extracted and given in the upper row in Fig.1(c). Besides the background light filling the whole demonstrated region, some apparent larger electric fields are confined to the surface of the probe for GPM probe, indicating that excited SPPs propagate along the conical surface. According to the distribution of the permittivity, the SPPs excitation

area should be between z = 2 μm to z = 3 μm. From the electric distribution, some of the SPPs propagate beyond its excitation area and towards the tip apex. When the SPPs propagate closer to the tip apex, the wavelength of the SPPs becomes shorter and the Ez component becomes stronger. Thus, nanofocusing effect similar to other tapered tips also occurs in this GPM probe. Further simulations show that as the radius of the probe becomes larger, the intensity of the SPPs gradually decreases to some extent and remains unchanged. The SPPs excitation and propagation on the probe surface can also be observed from the electric field distribution of the cross section (xy plane). Here, we give the amplitude distribution of the electric field, E, at plane z = 1.1 μm. The excitation and propagation of the SPPs on the probe surface with a GPM are verified again by the distribution of E. It is worth noting that the SPPs exist on the whole cross section rather than only the incident side. The difference between the incidence side and the opposite side is the intensity, of which the incident side is slightly stronger than the other one. Apart from the incident conditions, the field distribution is also determined by the electromagnetic eigenmode of the probe structure. As the eigenmode is axial symmetric, therefore, it is possible for the probe to support the SPPs existing on the whole cross section. As for the tip with constant negative permittivity, the counterparts of the electric field distributions are given in the right column of Fig.1(c). The electric field near the probe surface is not stronger than that at other areas. No SPPs are excited or propagate on the conical surface.

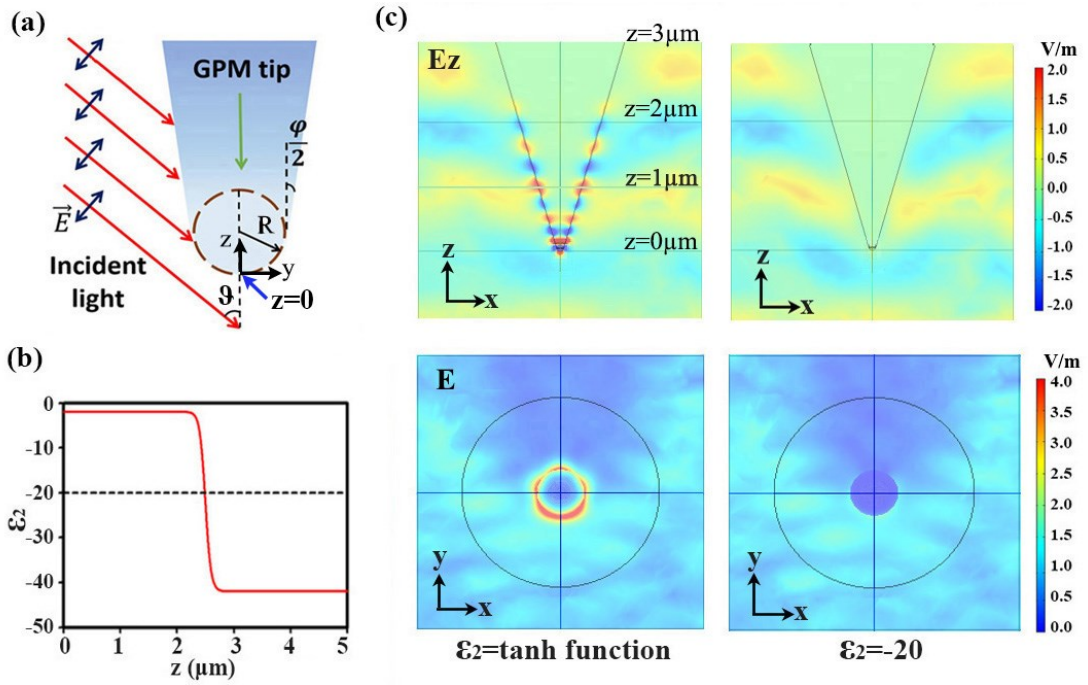

Fig. 1. (a) Schematic of a plasmonic probe made of a GPM and the incident light. (b) A gradient negative-permittivity distribution and a constant permittivity distribution inside a probe. (c) Distributions of electric component Ez and electric amplitude E for probes with a GPM (left column) and with a constant negative permittivity of -20 (right column).

3. Nanofocusing effect of the probe can be reinforced by the distribution of the probe permittivity

The above simulations demonstrate that SPPs are excited and propagate on a GPM probe surface without any excitation structure, and nanofocusing is achieved at the tip apex. The field enhancement and localization effect at the tip apex are influenced by two factors. One is the SPPs excitation efficiency, which is determined by the local permittivity of the tip, the permittivity gradient, and the length of the

SPPs excitation region. The other is the nanofocusing effect of the probe, which is determined by the geometric structure and the permittivity distribution of the probe. Here, we focus on the impact of the distribution of the permittivity on the nanofocusing effect.

The behavior of the SPPs propagating on a conical probe with constant negative permittivity has been theoretically analyzed [35]. Under certain hypotheses of $\theta \ll 1$ and $r \to 0$, (θ and r are the coordinates of the conical probe in a spherical coordinate system in which the origin of the spherical system is set at the vertex of the conical probe and the polar axis is set along the axis of the conical probe), the electric field components around the conical probe with permittivity of ε_2 and apex angle of φ can be obtained as

$$E_r = \frac{iAc\eta I_0(\eta\theta)}{\omega\varepsilon_2 r^{\frac{3}{2}}} e^{-i\sqrt{\eta^2-\frac{1}{4}}\ln\frac{r}{r_0}-i\omega t} (\theta \le \varphi/2) \quad (1)$$

$$E_\theta = \frac{-AcI_1(\eta\theta)}{\omega\varepsilon_2 r^{\frac{3}{2}}} \left(\frac{i}{2}+\sqrt{\eta^2-\frac{1}{4}}\right) e^{-i\sqrt{\eta^2-\frac{1}{4}}\ln\frac{r}{r_0}-i\omega t} (\theta \le \varphi/2) \quad (2)$$

$$E_r = \frac{-iBc\eta k_0(\eta\theta)}{\omega\varepsilon_1 r^{\frac{3}{2}}} e^{-i\sqrt{\eta^2-\frac{1}{4}}\ln\frac{r}{r_0}-i\omega t} (\theta \ge \varphi/2) \quad (3)$$

$$E_\theta = \frac{-Bck_1(\eta\theta)}{\omega\varepsilon_1 r^{\frac{3}{2}}} \left(\frac{i}{2}+\sqrt{\eta^2-\frac{1}{4}}\right) e^{-i\sqrt{\eta^2-\frac{1}{4}}\ln\frac{r}{r_0}-i\omega t} (\theta \ge \varphi/2) \quad (4)$$

where ε_1 is the permittivity of the free space; A and B are constants which can be determined by the boundary conditions; η is the separation constant introduced when solving the field distribution equation by the separation of variables method, which is also determined by the boundary conditions; I_0 (I_1), K_0 (K_1) are the zeroth (first) order modified Bessel and Hankel functions. From the phase distribution of the above electromagnetic fields, the phase velocity, group velocity and wave vector of the SPPs can be easily obtained as

$$v_p = v_g = -\frac{\omega r}{\sqrt{\eta^2-\frac{1}{4}}} \quad (5)$$

$$k = \frac{-\sqrt{\eta^2-\frac{1}{4}}}{r} \quad (6)$$

where the negative sign indicates that the SPPs propagate towards the tip apex.

From Equations (5) and (6), the propagation of SPPs through a conical structure exhibits inherent nanofocusing effect feature. When SPPs are propagating towards the apex, their group velocity and phase velocity decrease gradually while their wave vectors increase monotonously. When r approaches 0, the wave vector and propagating velocity tend to infinity and 0, respectively. Thus, the SPPs can hardly propagate forward, converting to LSP and oscillating at the tip apex. This physical process is the essence of the plasmonic super focusing effect of a conical plasmonic probe.

For Equations (1) - (4), the electromagnetic field distributions are not only determined by the structure itself, but also by the electromagnetic parameters of the probe material. Moreover, the wave vector and the propagating velocity can be tuned by the probe permittivity through parameter η. It means that it is possible to reinforce the nanofocusing effect by designing the permittivity distribution. From the boundary conditions, the relationship between η and ε_2 can be easily obtained,

$$\varepsilon_2 \frac{I_1(\eta\varphi/2)}{I_0(\eta\varphi/2)} = -\varepsilon_1 \frac{k_1(\eta\varphi/2)}{k_0(\eta\varphi/2)} \quad (7)$$

For a certain value of φ and ε_1, the material of the cone structure ε_2 determines the value of η uniquely. We numerically solve equation (7), then η as a function of ε_2 can be obtained. Fig.2(a) gives the plot of η as well as the wave vector varying with the permittivity ε_2 at r=1 μm, in calculation, φ

and ε_1 take values of 10 degree and 1, respectively. With the increase of ε_2, they both increase monotonically. When ε_2 approaches -1, the two parameters increase even dramatically, resulting in anomalous large η and $|k|$ values near the area $\varepsilon_2 = -1$. An anomalous large wave vector corresponds to a very small propagation speed of SPPs. Therefore, the energy of the SPPs will be localized near this area, resulting in an enhanced electric field. Fig.2(b) gives the plot of two components of the electric field as functions of the permittivity ε_2, both of which increase with the increase of ε_2. The two electric filed components dramatically increase when ε_2 approaches -1, where the field concentration effect can be regarded as another kind of nanofocusing effect. Moreover, the position of this field concentration effect can be tuned by adjusting the location of $\varepsilon_2 = -1$. When applying this field concentration effect to the apex of the probe, the nanofocusing effect of the conical structure will be reinforced greatly.

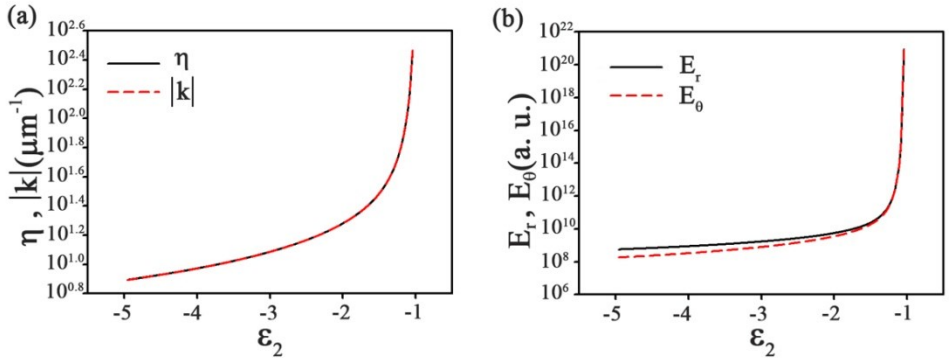

Fig. 2. (a) η and wave vector $|k|$. (b) Electric components as functions of the permittivity of the cone material ε_2 at r = 1 μm.

Now we design the distribution of the permittivity of the cone structure. Two nanofocusing effects are superposed to enhance the electromagnetic localization and enhancement effect at the tip apex. In order to obtain the field energy gathered at the tip apex, the permittivity at the apex should be designed to be -1. We suppose that the permittivity is a linear function of r, $\varepsilon_2 = -4r/r_0 - 1$, where r_0 is the unit length of 1 μm. As shown in Fig.3(a), ε_2 varies from -1 to -9 when r changes from 0 μm to 2 μm. Fig.3(b) and (c) give the plots of wave vector and electric components varying with the coordinate r. For comparison, the counter parts of a constant negative permittivity $\varepsilon_2 = -3$ are also given using a red color. In calculation, the range of r is taken from 0.01 μm to 2μm. With the decrease of r, both the wave vector and the electric field increase continuously. When r approaches 0.01 μm, the increasing trend becomes even more dramatic. It is worth noting that the increasing rate of linear permittivity is much greater than that of the constant permittivity, despite the similar growth trends of wave vector and electric field for linear and constant permittivity distribution. When r approaches 0.01 μm, the wave vector of the linear permittivity is several orders of magnitude higher than that of the constant permittivity. As for the electric field components, tens orders of magnitude higher than the constant permittivity is obtained. Apparently, the nanofocusing effect at the tip apex for the linear permittivity is enhanced dramatically.

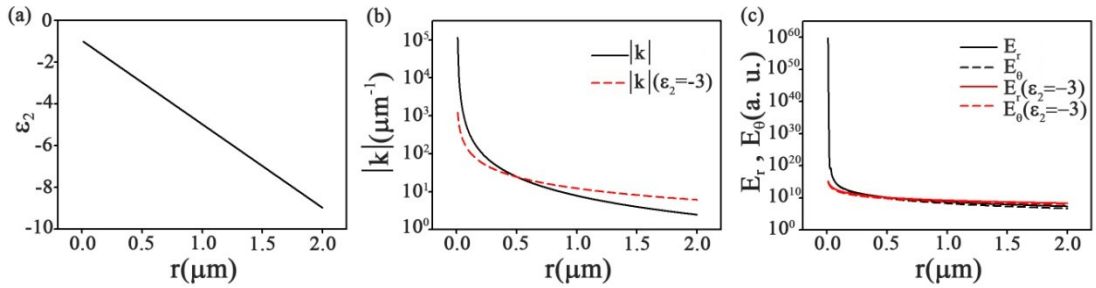

Fig. 3. (a) A linear distribution of the permittivity ε_2 near the probe apex from r = 0.01 μm to r = 2 μm. (b)Wave vectors as functions of r for the linear permittivity distribution in (a) and a constant permittivity ($\varepsilon_2 = -3$), respectively. (c) Electric field components as functions of r for the linear permittivity distribution and constant permittivity, respectively.

In the next step, we use numerical method to demonstrate the enhanced nanofocusing properties of a GPM probe. We still simulate the interaction between a GPM probe and a TM polarized incident beam shown as Fig.1(a). In order to coincide with the theoretical analysis, the apex angle of the probe decreases to $\varphi = 10$ degree, which meets the condition of $\theta \ll 1$, and the radius of the sphere connected with the cone decreases to R = 5 nm to match the approximation $r \to 0$. In order to achieve the same SPPs excitation efficiency as possible, we set the permittivity distributions with the same slope of $\beta = 5 \times 10^6/\mathrm{m}$, same span of $\delta = 20$, and same varying region center at z_0 = 0.5 μm. According to the permittivity distribution function $\varepsilon_2 = -\delta\tanh(\beta(z - z_0)) + \varepsilon_{r0}$, by changing the parameter ε_{r0}, we obtain different permittivity distributions inside the probe as well as at the tip apex. In addition, to make the calculation more convincible, we introduce an absorption loss to the GPM by adding an imaginary part of $\varepsilon_i = 0.02$ to the permittivity ε_2.

Fig. 4(a) depicts the amplitude of the electric field E at the tip apex as a function of the permittivity ε_2 (z = 0). Theoretically, the whole curve should present three different nanofocusing effects according to their different permittivity values at the tip apex. When the permittivity at the tip apex is much smaller than -1, the whole permittivity inside the probe is negative with a gradient, then SPPs are able to be excited and propagate towards the tip apex. As the permittivity at the tip apex is much smaller than -1, the field enhancement and localization effect cannot be reinforced greatly by the distribution of the permittivity. Thus, the nanofocusing effect mainly results from the conical structure, and the overall nanofocusing effect is not prominent. This condition corresponds to the left part of the curve (left side of the resonant peak) shown in Fig.4(a). Compared with the incident light, the electric field amplitude has been enhanced by about 200 times, and the nanofocusing effect does occur. However, it is far weaker than that of the resonant peak.

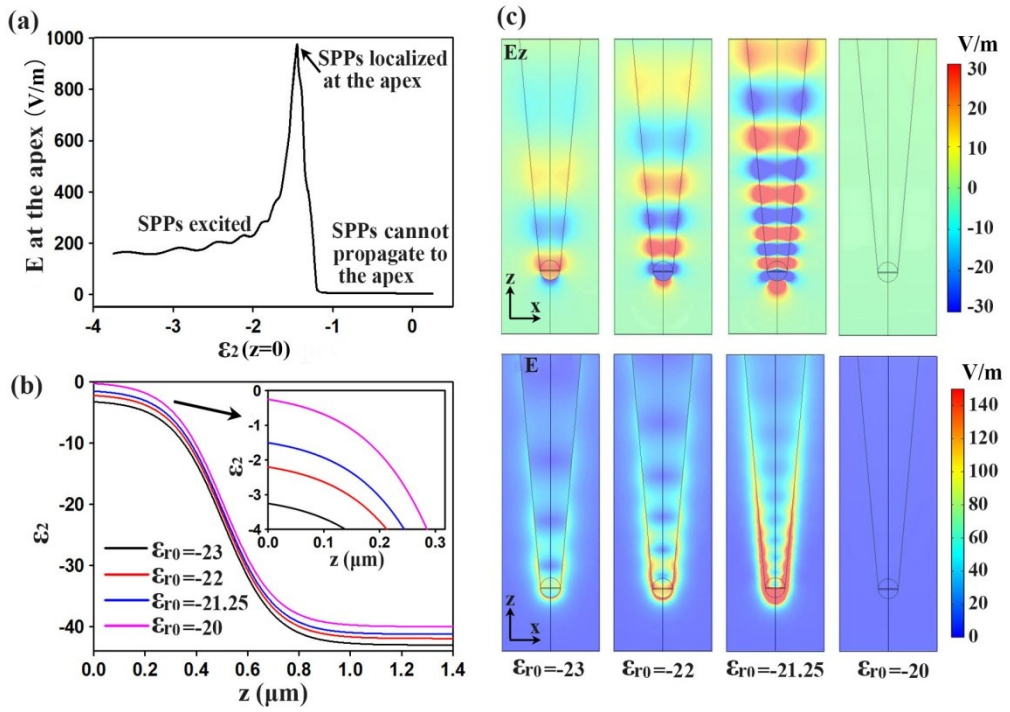

Fig. 4. Nanofocusing effect is obtained by designing the permittivity distribution inside the probe. (a) The electric amplitude E at the apex as a function of the permittivity at the tip apex ε_2 (z = 0 μm). (b) Several representative permittivity distributions inside the probe. (c)Several representative electric field distributions near the tip apex, where R = 5 nm, $\varphi = 10$ degree, $\beta = 5 \times 10^6/\mathrm{m}$, $\delta = 20$, $\varepsilon_i = 0.02$.

When the permittivity at the tip apex increases to near -1, SPPs can also be excited and propagate to the tip apex. In this condition, two kinds of nanofocusing effects, respectively resulting from the conical structure and permittivity distribution, will work together. Thus, a super nanofocusing effect will appear at $\varepsilon_2 = -1$. As shown in Fig.4(a), a sharp peak with the maximum electric amplitude around 1000 times larger than the incident light appears between $\varepsilon_2 = -2$ and -1. Theoretically, this resonance peak should appear at $\varepsilon_2 = -1$. However, when r approaches 0, the SPPs propagating on the opposite sides of the probe will couple with each other, leading to a long range or short range SPPs coupled mode. The closer the two opposite sides are, the stronger the coupled effect is. For the above simulated structure, the obtained coupled SPPs mode is short range SPPs, which can be identified through the symmetry of the electric field distribution. As for the short range SPPs, its wave vector becomes even greater with the decrease of r [39]. As a result, before the permittivity reaches - 1, the wave vector of the coupled SPPs has become large enough. Accordingly, their propagating speed becomes small enough and the electromagnetic energy is concentrated at the tip apex. When increasing the radius of the sphere R at the end of the cone, there will be a right shift of the peak position, which reaches -1 to the utmost extent when the radius becomes large enough.

As for the permittivity of the tip apex larger than -1, which is unable to support the propagating of the SPPs. Though SPPs can be excited at the area far from the tip apex (corresponding to a large value of z), they cannot reach the tip apex. Therefore, the electric field at the tip apex is almost zero. The flat part on the right side of the resonant peak corresponds to this condition.

The similar properties of the nanofocusing effect in Fig.4(a) can also be observed from the distribution of the electric field. We choose four representative points from the curve in Fig.4(a), which correspond to $\varepsilon_{r0} = -23, -22, -21.25, -20$, respectively. Fig.4(b) gives the permittivity distributions

as functions of z for these four points, the inset is the distribution near z = 0μm. Obviously, at the tip apex (z = 0μm), three of the four permittivity values are smaller than -1, thus SPPs can be excited and propagate to the probe apex, nanofocusing effect can be obtained. While the last one is larger than -1, for this condition, the excited SPPs cannot travel to the apex. Fig.4(c) shows the distributions of the electric field component Ez and amplitude E in the upper row and the lower row, respectively, for these four permittivity distributions. For the first three conditions, nanofocusing effects are all obtained, the fields at the tip apex are much stronger than that of the incident light. Among them, the focusing effect in the third one ($\varepsilon_{r0} = -21.25$) is obviously stronger than the first two because both nanofocusing mechanisms, as discussed above, contribute to the energy localization effect. As for the fourth electric distribution, there are SPPs excited above the apex, but they cannot reach the tip apex because the permittivity at the tip apex is larger than -1. Besides, as the permittivity of the tip apex is larger than -1, this probe doesn't possess the characteristics of a metal, LSPR and lightning rod effect resulting in the field enhancement at a metal probe will also disappear, leading to both small electric component Ez and the amplitude E.

4. Practical consideration and implementation of a GPM probe

To identify the practical performance of a GPM probe, we compare the nanofocusing effect of a GPM probe with a conventional noble metal probe made by gold (Au), because gold is the most used noble metal for fabricating SPM probes due to its high free electron density, strong LSP resonance effect and chemical stability in the visible region. We still use the probe structure and illumination conditions shown in Fig.1(a) to do simulation. In calculations, the permittivity distribution of the GPM probe is set to be $\varepsilon_2 = -\delta\tanh\big(\beta(z - z_0)\big) + \varepsilon_{r0}$, where $\delta = 5.5$, $\beta = 5 \times 10^6/\mathrm{m}$, $z_0 = 0$ μm, $\varepsilon_{r0} = -1.05$. We keep the real part of the permittivity distribution unchanged and adjust the imaginary part of the permittivity from 0.05 to 0.5 to introduce different material loss. For different absorption, we extract electric field magnitude distributions along the x direction at $z = 0$, as shown in Fig.5. When the imaginary part of the permittivity increases, the electric field magnitude of the peak decreases. For comparison, we also give the electric field distribution at the same position of an Au probe with the same geometry, as shown by the red solid line. Obviously, at low absorption, e.g., $\varepsilon_i = 0.05$, the peak electric field magnitude of the GPM probe is about 140 V/m, which is much stronger than that of an Au probe. Even at high absorption, e.g., $\varepsilon_i = 0.5$, the peak electric field magnitude is still 5 times larger than that of the incident light, corresponding to a 25-fold intensity enhancement, while at the center, its electric field is still slightly stronger than that of an Au probe. This implies that the nanofocusing effect of a GPM probe has great tolerance to absorption loss and its field enhancement effect is much better than an Au probe with the lightning rod effect.

Besides the field enhancement, spatial resolution is another important factor which impact the performance of a probe. It has been predicted that the spot size of the confined light near the tip apex typically determines the spatial resolution. The smaller the spot size is, the higher the spatial resolution is. Here, we use the full width at half maximum (FWHM) to represent the spot size. From the electric field distribution in Fig.5, it is clearly seen that while the FWHM of the GPM probe decreases with the decrease of the absorption, the FWHM of the GPM probe for all the absorptions from 0.05 to 0.5 are smaller than that of the Au probe. It demonstrates that the spatial resolution of a GPM probe is better than that of an Au probe. The insets in Fig.5 are the electric field amplitude distributions near the tip apex. The upper one is that of the GPM probe with $\varepsilon_i = 0.05$ and the lower one corresponds to the Au probe. The electric field of the GPM probe is much stronger than that of an Au probe. Besides, for the GPM probe, its light energy is almost confined near the tip apex, resulting in a very small spot size.

While for the Au tip, the light is more decentralized, the spot size almost covers the whole arc range of the sphere. Therefore, in practical application, using a GPM probe, both the field enhancement and the spatial resolution will be improved greatly.

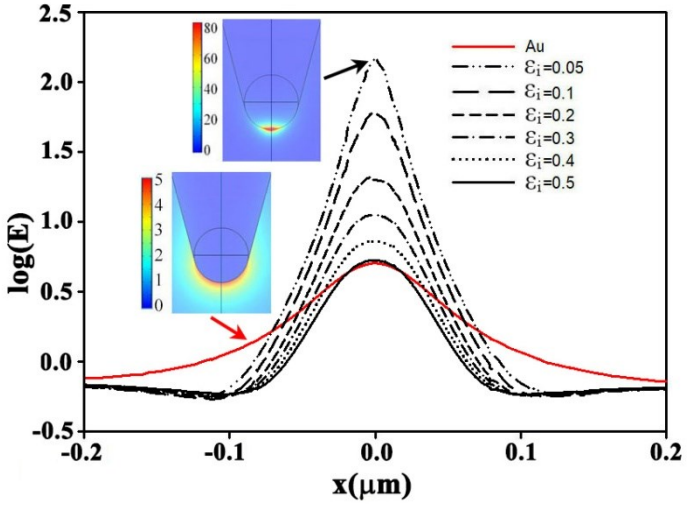

Fig. 5. Comparison of the nanofocusing effect between a GPM probe and an Au probe with the same geometry, electric field magnitude distributions along the x direction at z = 0 μm for different imaginary parts of the permittivity.

GPM probes can be fabricated by doped semiconductors. Though noble metals are the top choices for SPM in visible and near-infrared span, they are lossy resonators in the mid-infrared owing to their high electron concentration and inter-/intraband transitions. In contrast, doped semiconductor has been reported to be a reliable mid- infrared plasmon host by overcoming the losses seen in conventional metallic plasmonic materials. In addition, with the development of advanced fabrication techniques, materials with gradient permittivity can be readily obtained. For example, through monolayer doping, the distribution of dopants in indium arsenide (InAs) is fully controllable [40]. We will use InAs doped with silicon (Si) dopant grown by molecular beam epitaxy (MBE) on an InAs substrate to realize GPMs. The doping rate during the epitaxy process can be accurately controlled by tuning the temperature of the dopant cell to achieve any designed doping gradient. After growth, we will have a layer of GPM with several microns thickness. GPM probes can be fabricated by post-growth isotropic etching method. To model such structure, we assign a carrier concentration distribution of $n(z) = n_{min} + (n_{max} - n_{min})\tanh(\beta z)$ to a layer of monotonously doped InAs, where n_{max} and n_{min} are the maximum and minimum carrier concentration, respectively, and $\beta = 5 \times 10^6/\mathrm{m}$. The permittivity of this doped InAs can be described by the Drude model as following [41]:

$$\varepsilon_{InAs}(\omega, z) = \varepsilon_{\infty-InAs} - \frac{\omega_p^2(z)}{\omega^2 + i\omega\gamma} \tag{8}$$

where $\varepsilon_{\infty-InAs} = 12.3$ is the high frequency dielectric constant and γ is the collision frequency. $\omega_p = \sqrt{n(z)e^2/m^*\varepsilon_0}$ describes the plasma frequency of InAs, where e is the electric charge, m* is the electron effective mass, and ε_0 is the vacuum permittivity. For heavily doped semiconductors, γ and m* are also dependent on carrier concentration and their values are taken from the literature [42, 43]. Using the above model, the distribution of permittivity is determined by carrier concentration uniquely. We plot a series of permittivity distributions at different frequencies (wavelengths) for a given carrier concentration distribution of $n_{min} = 1.0\times10^{25}/\mathrm{m}^3$ and $n_{max} = 2.5\times10^{25}/\mathrm{m}^3$. The solid curve in Fig.6(a) shows the gradient distribution of the carrier concentration and Fig.6(b) shows the corresponding real and imaginary parts of the permittivity at different wavelengths, respectively.

Using the probe geometric structure in Fig.1(a), we also simulate the nanofocusing effect of a probe made of the above doped InAs. Figure 6(c) shows the electric field amplitude at the tip apex as a function of incident wavelengths for a probe with three different carrier concentration distributions, where the three curves correspond to n_{min} = $1.0\times10^{25}/m^3$, $1.1\times10^{25}/m^3$, $1.2\times10^{25}/m^3$, respectively, with the same variation range of the carrier concentration of n_{max} - n_{min} = $1.5\times10^{25}/m^3$. For each doping distribution, there is a sharp electric field peak appearing at one wavelength. While the real absorption of the material is included in this simulation, the maximum electric field at the tip apex is still more than 1100 times of the incident field. The field enhancement is much stronger than that of an Au probe with the same probe structure and under the same illumination, depicted by the red dashed line. Outside the resonant region, when the GPM does not possess metallic properties, the field strength of the Au tip apex is slightly larger than that of the GPM probe, as shown at the left end of the curves. While for the right part of curves, the electric field at the GPM tip apex is still larger than that of the Au probe, where SPPs are excited. However, the focusing effect is mainly contributed by the dispersion relation of the structure itself. The electric field distributions near the tip apex are also given in the insets of Fig.6(c), where the left one depicts the field distribution of the doped InAs probe with n_{min} = $1.0\times10^{25}/m^3$ and n_{max} = $2.5\times10^{25}/m^3$, the right one is for the Au probe at the same wavelength of 14.1 μm. It is clear that the doped semiconductor probe has much higher field enhancement and smaller spot size than that of the lighting rod effect at the tip apex, making it more sensitive both in spectral and spatial resolution.

To compare with probes utilizing LSPR at mid-infrared wavelengths, we use constantly doped InAs to demonstrate LSPR probes. While the same probe geometric structure is used, the doping concentration changes abruptly from higher to lower at the location of z = 0.5 μm (dashed curve in Fig.6(a)). Therefore, we may consider the InAs apex from z = 0.5 μm to z = 0 μm as a nanoparticle with a doping concentration of n_{lower} = $2\times10^{25}/m^3$. Its wavelength-dependent electric field is shown in Fig.6(d). The two peaks, A and B, are related to LSPR modes, which have different electric field distributions as shown in the insets. A series of simulations demonstrating various LSPR probes with various doping concentrations are shown in Fig.6(e). The highest amplitude enhancement near 14 μm is around 400, about 3 times lower than that of GPM probes. And the FWHM of electric field for LSPR probes is about 0.1μm, bigger than the 0.06 μm for GPM probes. This proves that our GPM probe has better performance than probes with solo LSPR effect, both higher concentrated electric field and smaller spot size. All the simulation results demonstrate strong evidence that using a doped semiconductor to make a GPM probe is a feasible way to enhance the performance of a probe for s-SNOM.

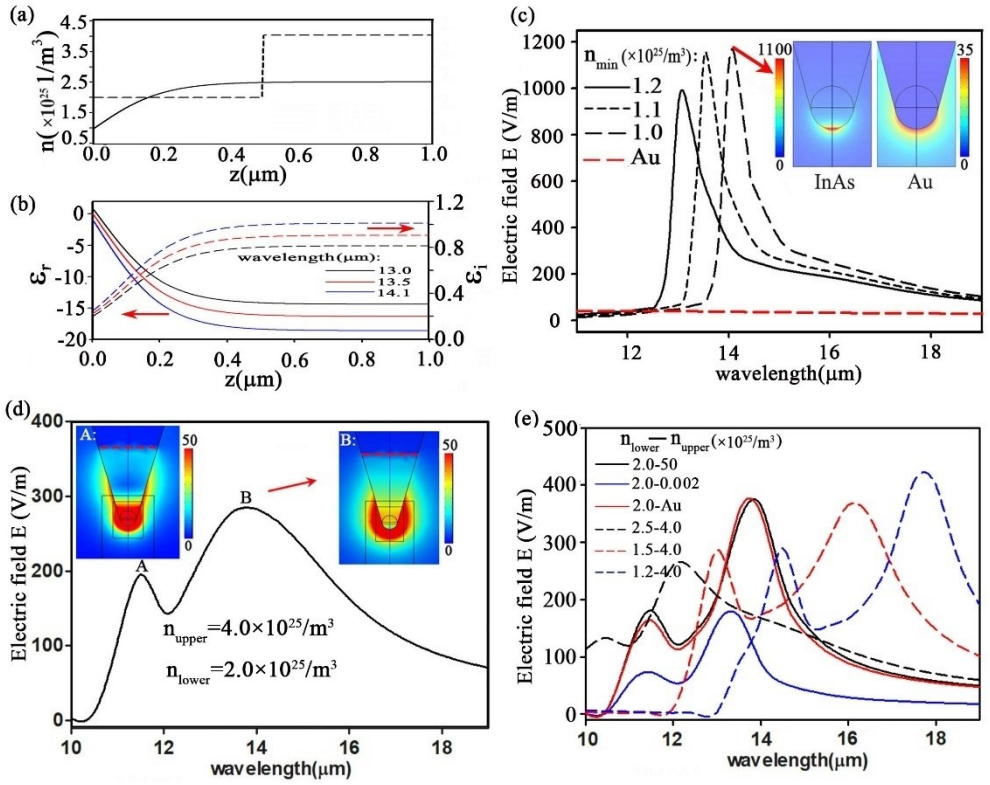

Fig. 6 (a) The distribution of the carrier concentration in a GPM probe (solid) and a LSPR probe (dashed) made by InAs. (b) Real and imaginary parts of the permittivity at different wavelengths for gradient carrier concentration distribution. (c) Electric field magnitude at the tip apex as a function of incident wavelength for GPM probes with three different doping distributions and an Au probe. The insets are the electric field distribution near the tip apex for a doped InAs probe with $n_{min} = 1.0\times10^{25}/m^3$ and $n_{max} = 2.5\times10^{25}/m^3$ and an Au probe at the wavelength of 14.1 μm. (d) Electric field magnitude at the tip apex as a function of incident wavelength for a LSPR probe. The insets show electric field distributions near the tip apex at two resonant wavelengths A and B. The red dashes denote the location of z = 0.5 μm. (e) Electric field magnitude at the tip apex of various LSPR probes with different doping concentrations.

5. Conclusions

In this paper, we explore a new avenue to improve the performance of s-SNOM probes by designing the permittivity distribution of probe materials rather than structural design. In our proposed GPM plasmonic probe, SPPs can be excited on its surface without any extra excitation structure and its original nanofocusing effect can be further enhanced dramatically by designing the probe permittivity distribution. For practical application considerations, the performances of GPM probes, a conventional Au probe, and LSPR probes are compared. Both the field enhancement and localization effects of the GPM probes are much better than those of an Au probe and LSPR probes. Moreover, a probe made of doped semiconductors promises a feasible way to make a GPM probe with excellent performance.

Funding. National Nature Science Foundation of China (11504336); Fundamental Research Funds for the Central Universities (2652017148); National Science Foundation (2102027); University of Delaware General University Research(20A00953).

References

[1] N. Rotenberg and L. Kuipers 2014 Mapping nanoscale light fields *Nat. Photonics* **8** 919-926

[2] P. Verma 2017 Tip-Enhanced Raman Spectroscopy: Technique and Recent Advances *Chem. Rev.* **117** 6447-6466

[3] J. A. Schuller, E. S. Barnard, W. Cai, Y. C. Jun, J. S. White and M. L. Brongersma 2010 Plasmonics for extreme light concentration and manipulation *Nat. Mater.* **9** 193-204

[4] C. Chen, N. Hayazawa and S. Kawata 2014 A 1.7 nm resolution chemical analysis of carbon nanotubes by tip-enhanced Raman imaging in the ambient *Nat. Commun.* **5** 3312

[5] K. Minn, B. Birmingham and Z. Zhang 2020 New development of nanoscale spectroscopy using scanning probe microscope *J Vac Sci Technol A* **38** 030801

[6] J. Mathurin, E. Pancani, A. Deniset-Besseau, K. Kjoller, C. B. Prater, R. Gref and A. Dazzi 2018 How to unravel the chemical structure and component localization of individual drug-loaded polymeric nanoparticles by using tapping AFM-IR *Analyst* **143** 5940-5949

[7] Z. Yang, J. Aizpurua and H. Xu 2009 Electromagnetic field enhancement in TERS configurations *J Raman Spectrosc* **40** 1343-1348

[8] T. Huang, S. Huang, M. Li, Z. Zeng, X. Wang and B. Ren 2015 Tip-enhanced Raman spectroscopy: tip-related issues *Anal. Bioanal. Chem.* **407** 8177-8195

[9] L. Meng, T. Huang, X. Wang, S. Chen, Z. Yang and B. Ren 2015 Gold-coated AFM tips for tip-enhanced Raman spectroscopy: theoretical calculation and experimental demonstration *Opt. Express* **23** 13804-13813

[10] A. Taguchi, N. Hayazawa, Y. Saito, H. Ishitobi, A. Tarun and S. Kawata 2009 Controlling the plasmon resonance wavelength in metal-coated probe using refractive index modification *Opt. Express* **17** 6509-6518

[11] B. Ren, G. Picardi and B. Pettinger 2004 Preparation of gold tips suitable for tip-enhanced Raman spectroscopy and light emission by electrochemical etching *Rev. Sci. Instrum.* **75** 837-841

[12] M. Asghari-Khiavi, B. R. Wood, P. Hojati-Talemi, A. Downes, D. McNaughton and A. Mechler 2012 Exploring the origin of tip-enhanced Raman scattering; preparation of efficient TERS probes with high yield *J Raman Spectrosc* **43** 173-180

[13] J. Li, J. Mu, B. Wang, W. Ding, J. Liu, H. Guo, W. Li, C. Gu and Z. Li 2014 Direct laser writing of symmetry-broken spiral tapers for polarization-insensitive three-dimensional plasmonic focusing *Laser Photonics Rev.* **8** 602-609

[14] B. N. Tugchin, N. Janunts, A. E. Klein, M. Steinert, S. Fasold, S. Diziain, M. Sison, E. B. Kley, A. Tünnermann and T. Pertsch 2015 Plasmonic Tip Based on Excitation of Radially Polarized Conical Surface Plasmon Polariton for Detecting Longitudinal and Transversal Fields *Acs Photonics* **2** 1468-1475

[15] F. Lu, W. Zhang, M. Liu, L. Zhang and T. Mei 2020 Tip-Based Plasmonic Nanofocusing: Vector Field Engineering and Background Elimination *IEEE J Sel Top Quantum Electron* **27** 1-12

[16] M. Liu, F. Lu, W. Zhang, L. Huang, S. Liang, D. Mao, F. Gao, T. Mei and J. Zhao 2019 Highly efficient plasmonic nanofocusing on a metallized fiber tip with internal illumination of the radial vector mode using an acousto-optic coupling approach *Nanophotonics* **8** 921-929

[17] N. Kazemi-Zanjani, S. Vedraine and F. Lagugné-Labarthet 2013 Localized enhancement of electric field in tipenhanced Raman spectroscopy using radially and linearly polarized light *Opt. Express* **21** 25271-25276

[18] M. Sun, Y. Fang, Z. Yang and H. Xu 2009 Chemical and electromagnetic mechanisms of tip-enhanced Raman scattering *Phys. Chem. Chem. Phys.* **11** 9412-9419

[19] I. Notingher and A. Elfick 2005 Effect of Sample and Substrate Electric Properties on the Electric Field Enhancement at the Apex of SPM Nanotips *J. Phys. Chem. B* **109** 15699-15706

[20] A. Downes, D. Salter and A. Elfick 2006 Finite Element Simulations of Tip-Enhanced Raman and Fluorescence Spectroscopy *J. Phys. Chem. B* **110** 6692-6698

[21] L. Wang and X. Xu 2007 High transmission nanoscale bowtie-shaped aperture probe for near-field optical imaging *Appl. Phys. Lett.* **90** 261105

[22] J. N. Farahani, D. W. Pohl, H. J. Eisler and B. Hecht 2005 Single Quantum Dot Coupled to a Scanning Optical Antenna: ATunable Superemitter *Phys. Rev. Lett.* **95** 017402

[23] T. L. Vasconcelos, B. S. Archanjo, B. S. Oliveira, R. Valaski, R. C. Cordeiro, H. G. Medeiros, C. Rabelo, A. Ribeiro, P. Ercius, C. A. Achete, A. Jorio and L. G. Cançado 2018 Plasmon-Tunable Tip Pyramids: Monopole Nanoantennas for Near-Field Scanning Optical Microscopy *Adv. Opt. Mater.* **6** 1800528

[24] H. Miranda, C. Rabelo, T. L. Vasconcelos, L. G. Cançado and A. Jorio 2020 Optical Properties of Plasmon-Tunable Tip Pyramids for Tip-Enhanced Raman Spectroscopy *Phys Status Solidi Rapid Res Lett* **14** 2000212

[25] A. Taguchi, J. Yu, P. Vermaa and S. Kawata 2015 Optical antennas with multiple plasmonic nanoparticles for tip-enhanced Raman microscopy *Nanoscale* **7** 17424-17433

[26] X. Yin, P. Shi, A. Yang, L. Du and X. Yuan 2020 Surface plasmon coupled nano-probe for near field scanning optical microscopy *Opt. Express* **28** 14831-14838

[27] S. S. Pal, S. K. Mondal, P. P. Bajpai and P. Kapur 2012 Optical fiber tip for field-enhanced second harmonic generation *Opt. Lett.* **37** 4017-4019

[28] S. K. Mondal, Member, A. Mitra, N. Singh, F. Shi and P. Kapur 2011 Ultrafine fiber tip etched in hydrophobic polymer coated tube for near-field scanning plasmonic probe *IEEE Photon. Technol. Lett.* **23** 1382-1384

[29] T. L. Vasconcelos, B. S. Archanjo, B. Fragneaud, B. S. Oliveira, J. Riikonen, C. Li, D. S. Ribeiro, C. Rabelo, W. N. Rodrigues, A. Jorio, C. A. Achete and L. G. Cancado 2015 Tuning Localized Surface Plasmon Resonance in Scanning Near-Field Optical Microscopy Probes *ACS nano* **9** 6297-6304

[30] C. Ropers, C. C. Neacsu, T. Elsaesser, M. Albrecht, M. B. Raschke and C. Lienau 2007 Grating-Coupling of Surface Plasmons onto Metallic Tips: A Nanoconfined Light Source *Nano Lett.* **7** 2784-2788

[31] S. Berweger, J. M. Atkin, R. L. Olmon and M. B. Raschke 2010 Adiabatic Tip-Plasmon Focusing for Nano-Raman Spectroscopy *J. Phys. Chem. Lett.* **1** 3427-3432

[32] J. R. Han, C. Chi, L. D. Zheng, C. H. Chun, C. J. You and Y. T. Jen 2018 Near-Field Plasmonic Probe with Super Resolution and High Throughput and Signal-to-Noise Ratio *Nano Lett.* **18** 881-885

[33] F. D. Angelis, G. Das, P. Candeloro, M. Patrini, M. Galli, A. Bek, M. Lazzarino, I. Maksymov, C. Liberale, L. C. Andreani and E. D. Fabrizio 2010 Nanoscale chemical mapping using three-dimensional adiabatic compression of surface plasmon polaritons *Nat. Nanotechnol.* **5** 67-72

[34] S. Kim, N. Yu, X. Ma, Y. Zhu, Q. Liu, M. Liu and R. Yan 2019 High external-efficiency nanofocusing for lens-free near-field optical nanoscopy *Nat. Photonics* **13** 636-643

[35] A. J. Babadjanyan, N. L. Margaryan and K. V. Nerkararyan 2000 Superfocusing of surface polaritons in the conical structure *J. Phys. D* **87** 3785-3788

[36] M. I. Stockman 2004 Nanofocusing of Optical Energy in Tapered Plasmonic Waveguides *Phys. Rev. Lett.* **93** 137404

[37] X. Wang, Y. Deng, Q. Li, Y. Huang, Z. Gong, K. B. Tom and J. Yao 2016 Excitation and propagation of surface plasmon polaritons on a non-structured surface with a permittivity gradient *Light Sci. Appl.* **5** e16179

[38] H. Gao, E. Herrmann and X. Wang 2020 Programmable field localization and enhancement effects on a non-structured planar surface with a permittivity gradient *Opt. Express* **28** 1051-1060

[39] P. Berini 2009 Long-range surface plasmon polaritons *Adv. Opt. Photonics* **1** 484-588

[40] J. C. Ho, A. C. Ford, Y. Chueh, P. W. Leu, O. Ergen, K. Takei, G. Smith, P. Majhi, J. Bennett and A. Javey 2009 Nanoscale doping of InAs via sulfur monolayers *Appl. Phys. Lett.* **95** 072108

[41] M. Fox 2002 Optical properties of solids *Am. J. Phys.* **70** 1269-1270

[42] S. Law, L. Yu and D. Wasserman 2013 Epitaxial growth of engineered metals for mid-infrared plasmonics *J Vac Sci Technol B* **31** 03C121

[43] S. Law, D. C. Adams, A. M. Taylor and D. Wasserman 2012 Mid-infrared designer metals *Opt. Express* **20** 12155-12165